NANOSYSTEMS:
PHYSICS, CHEMISTRY, MATHEMATICS

Original article

Kiryanov N.V., Martinson K.D. *Nanosystems: Phys. Chem. Math.*, 2025, **16** (6), 818–828.
http://nanojournal.ifmo.ru
DOI 10.17586/2220-8054-2025-16-6-818-828

Effect of fuel-to-oxidizer ratio on the structural and magnetic properties of $Zn_{0.5}Mn_{0.5}Fe_2O_4$ nanoferrites synthesized via glycine-nitrate combustion

Nikita V. Kiryanov[1], Kirill D. Martinson[2]

[1]St. Petersburg Electrotechnical University "LETI", St. Petersburg, 199026, Russia
[2]Ioffe Institute, Politekhnicheskaya st., 26, St. Petersburg, 194064, Russia

Corresponding author: Nikita V. Kiryanov, nikyr@mail.ru

PACS 61.46Df, 75.50.Gg, 75.75.Fk

ABSTRACT Nanostructured $Zn_{0.5}Mn_{0.5}Fe_2O_4$ ferrites were synthesized by the glycine–nitrate solution combustion method with the fuel-to-oxidizer ratio f varied from 0.4 to 1.6 in order to clarify the influence of redox conditions on structure and magnetic properties. X-ray diffraction confirms the formation of single-phase cubic spinel for all compositions, with the crystallite size changing from $\sim$ 8 to 108 nm and the minimum values of both crystallite size and lattice parameter (8.420 Å) obtained under fuel-deficient conditions ($f = 0.4$); the lattice microstrain does not exceed 0.5 %. SEM observations reveal 3 – 5 μm agglomerates composed of 30 – 190 nm particles, while EDX analysis shows cation ratios close to the nominal composition. Magnetic measurements at 300 K demonstrate typical soft-magnetic behavior with saturation magnetization ranging from 16.1 to 68.3 emu/g, residual magnetization from 1.8 to 20.3 emu/g and coercive force from 34.7 to 85.6 Oe, all efficiently tuned by the fuel content. The highest saturation magnetization is achieved near the stoichiometric regime (f $\approx 0.8 - 1.0$), whereas fuel-rich mixtures result in increased coercivity due to microstructural refinement and lattice strain. The established correlations between combustion conditions, structural parameters and magnetic response show that controlled variation of the fuel ratio is an effective tool for tailoring Zn–Mn ferrite nanopowders for low-loss soft-magnetic applications.

KEYWORDS Zn-Mn ferrites, solution combustion, fuel-to-oxidizer ration, crystal structure, microstructure, magnetic properties, soft magnetic materials

ACKNOWLEDGEMENTS The authors of the article express their gratitude to the Institute of Applied Materials Science of the Joint-Stock Company "Almaz Antej – Obuhovskij zavod" for assistance in conducting the study of morphology and structure.

FOR CITATION Kiryanov N.V., Martinson K.D. Effect of fuel-to-oxidizer ratio on the structural and magnetic properties of $Zn_{0.5}Mn_{0.5}Fe_2O_4$ nanoferrites synthesized via glycine-nitrate combustion. *Nanosystems: Phys. Chem. Math.*, 2025, **16** (6), 818–828.

1. Introduction

Manganese-zinc ferrites are among the most widely used soft magnetic materials owing to their high initial permeability, relatively large saturation magnetization, high electrical resistivity and low core losses in the low- and medium-frequency ranges [1, 2]. These properties make Mn–Zn ferrites indispensable for electromagnetic components such as power transformers, inductors, electromagnetic interference (EMI) filters, read-write heads and antenna cores in both civil and military electronics [3]. In addition to traditional bulk components, Mn–Zn ferrite nanopowders are increasingly considered for microwave absorbers, ferrofluids and biomedical systems, where the combination of moderate magnetization, chemical stability and low toxicity is especially attractive [4–6].

It is now well recognized that the magnetic performance of spinel ferrites is strongly governed not only by their chemical composition, but also by cation distribution between A and B sublattices, crystallite size, porosity and grain-boundary characteristics [7]. When the characteristic size of ferrite particles approaches the single-domain range, changes in coercivity, saturation magnetization and loss behaviour are observed because of surface spin disorder and the increasing role of magnetocrystalline anisotropy [8]. Therefore, the development of reliable routes for synthesizing nanosized Mn–Zn ferrites with controlled particle size distribution and minimal secondary phases remains a key issue for tuning their functional properties and for decreasing the sintering temperature in ceramic processing [9, 10].

A variety of wet-chemical techniques have been proposed to produce ferrite nanopowders, including sol-gel and Pechini routes, co-precipitation, hydrothermal and solvothermal synthesis, microemulsion methods and different types of combustion approaches [11–14]. Conventional solid-state ceramic methods, while technologically simple, typically require high calcination temperatures and prolonged heat treatments, which often lead to coarse grains, broad size distributions and inhomogeneous cation distribution [15]. Wet-chemical routes usually provide better mixing at the molecular

level and lower synthesis temperatures, but they may suffer from complicated multi-step procedures, the need for complexing agents or surfactants, and difficulties in scaling up [16].

Among these techniques, solution combustion synthesis has attracted particular attention as a simple, low-cost and energy-efficient route for producing nanosized oxide powders [17]. In this method, aqueous solutions containing oxidizing metal nitrates and an organic fuel are ignited to initiate a self-sustaining exothermic reaction that yields the desired oxide product within a few seconds [18]. The high local temperature and rapid gas evolution during combustion typically produce highly porous, weakly agglomerated powders composed of fine crystallites, while the intimate mixing in the precursor solution ensures good chemical homogeneity [19]. For ferrite systems, solution combustion offers additional advantages of short synthesis time, easy control of stoichiometry and the possibility of tailoring the microstructure by adjusting the composition of the reactive mixture [20, 21].

Glycine is one of the most commonly used fuels in nitrate-based combustion systems because it can simultaneously act as a fuel, a complexing agent and a dispersant [22–24]. The so-called glycine-nitrate process allows effective chelation of metal cations, which reduces segregation and facilitates the formation of single-phase spinel ferrites at relatively low post-combustion temperatures [25]. Nevertheless, the characteristics of the resulting nanopowders strongly depend on the redox balance of the reacting system, usually expressed by the fuel-to-oxidizer ratio (Red/Ox ratio or f value) [26]. This parameter governs the adiabatic combustion temperature, the number of gaseous products released and the flame propagation rate, thereby affecting the crystallite size, morphology, defect structure and even the cation distribution in the final oxide [27, 28].

Several studies have reported the synthesis of Mn–Zn ferrites by different combustion routes using urea, glycine, citric acid and other fuels [29–31]. It has been shown that the choice of fuel and the calcination conditions significantly influence the structural and magnetic properties, including saturation magnetization, coercivity and Curie temperature. However, in many works the fuel content is fixed close to the stoichiometric value, and only limited information is available on how systematic variation of the Red/Ox ratio affects the structural parameters and magnetic behaviour of Mn–Zn ferrite nanopowders, especially in the glycine–nitrate system. Existing reports mainly focus either on phase formation and crystallite size or on magnetic properties, without establishing a clear correlation between combustion conditions, structural peculiarities and macroscopic magnetization characteristics [32, 33].

The composition $Zn_{0.5}Mn_{0.5}Fe_2O_4$ is of particular interest among Mn–Zn ferrites, since it lies in the concentration range where high saturation magnetization and low losses can be combined with relatively high electrical resistivity [34]. In the nanoscale state, $Zn_{0.5}Mn_{0.5}Fe_2O_4$ can exhibit size-dependent transitions between multi-domain, single-domain and superparamagnetic regimes, which are attractive for applications in high-frequency absorbers, magnetic recording media and biomedical hyperthermia [35]. At the same time, the non-equilibrium conditions inherent to combustion synthesis may alter the Mn^{2+}/Mn^{3+} and Fe^{2+}/Fe^{3+} ratios and redistribute cations between tetrahedral and octahedral sites, thus providing an additional tool for tailoring the magnetic response [36].

Therefore, a detailed study of how the Red/Ox ratio in glycine-nitrate combustion affects the formation of $Zn_{0.5}Mn_{0.5}Fe_2O_4$ nanopowders, their microstructure and magnetic properties is both fundamentally and practically important. By establishing such correlations, it becomes possible to optimize synthesis parameters for obtaining nanopowders with the required combination of crystallite size, lattice parameter and magnetic characteristics for specific device applications [37].

In this work, nanostructured $Zn_{0.5}Mn_{0.5}Fe_2O_4$ powders were synthesized via the glycine-nitrate solution combustion method with the fuel-to-oxidizer ratio f varied from 0.4 to 1.6, where $f = 1.0$ corresponds to the stoichiometric composition of the redox mixture. The structural properties were investigated by X-ray diffraction and Rietveld refinement, including the evaluation of crystallite size, lattice parameter and lattice strain. The morphology and particle size distributions were studied using scanning electron microscopy and image analysis, and the cation composition was verified by energy-dispersive X-ray spectroscopy. Finally, the magnetic behaviour at room temperature was examined by vibrating-sample magnetometry in fields up to 400 Oe in order to determine saturation magnetization, residual magnetization and coercive field. The results obtained make it possible to elucidate the role of combustion redox conditions in controlling the structural evolution and magnetic response of Zn–Mn ferrite nanopowders and to propose guidelines for the design of soft magnetic materials synthesized by solution combustion routes.

2. Experimental

$Zn_{0.5}Mn_{0.5}Fe_2O_4$ nanoparticles were synthesized by the glycine-nitrate solution combustion method. Zinc nitrate hexahydrate $Zn(NO_3)_2{\cdot}6H_2O$, manganese nitrate hexahydrate $Mn(NO_3)_2{\cdot}6H_2O$ (99.99 %), iron(III) nitrate nonahydrate $Fe(NO_3)_3{\cdot}9H_2O$ (99 %), glycine CH_2NH_2COOH and nitric acid HNO_3 were used as starting reagents without further purification. The required molar amounts of metal nitrates corresponding to the nominal composition $Zn_{0.5}Mn_{0.5}Fe_2O_4$ were weighed and dissolved in 50 mL of distilled water to obtain precursor solutions for 1 g of oxide powder. To ensure complete dissolution of the crystalline hydrates and to avoid precipitation of basic salts, 5 mL of 5 M HNO_3 were slowly added under vigorous magnetic stirring. The total oxidizing and reducing valences of nitrates and glycine were calculated according to the conventional propellant chemistry approach, and the amount of fuel was adjusted to obtain fuel-to-oxidizer ratios $f = 0.4$, 0.6, 0.8, 1.0, 1.2, 1.4 and 1.6, where $f = 1.0$ corresponds to the stoichiometric redox

composition. The as-prepared solutions were continuously stirred for 20 – 30 min until a clear homogeneous sol was obtained.

For combustion synthesis, each precursor solution was transferred into a cylindrical porcelain crucible and heated on a hot plate up to ∼200 °C to evaporate the excess water and form a viscous gel. Further heating initiated self-sustained combustion, which proceeded rapidly throughout the volume of the gel, accompanied by the release of large amounts of gaseous products and the formation of a voluminous, highly porous ash. No external oxidizing atmosphere was supplied; the reaction was carried out in air at ambient pressure. The as-combusted powders were gently crushed in an agate mortar and subsequently homogenized in a vibratory mill for 30 min to break soft agglomerates and to obtain a more uniform particle size distribution. In order to remove possible residual carbon and to improve crystallinity, the powders were additionally calcined in air at 600 °C for 2 h with a heating rate of 5 °C/min and then cooled to room temperature inside the furnace.

Phase composition and structural parameters of the synthesized powders were investigated by X-ray diffraction (XRD). Diffraction patterns were collected at room temperature on a Bruker D2 Phaser diffractometer using monochromatic Co-Kα radiation ($\lambda = 1.7903$ Å) operated at 30 kV and 10 mA. The data were recorded in the 2θ range from 10° to 80° with a step of 0.02° and a counting time of 1 s per step. The raw diffraction profiles were corrected for background and instrumental broadening before further analysis. The crystal structure was refined assuming a cubic spinel phase with space group $Fd\bar{3}m$. The lattice constant a, average crystallite size D and microstrain β were determined using the Topas software package by profile fitting of the most intense reflections (220), (311), (400), (422), (511) and (440). The values of D were obtained from the integral breadth of the diffraction peaks, taking into account both size and strain broadening contributions.

The morphology of the combustion-derived powders and the size of individual particles were examined by scanning electron microscopy (SEM) on a Tescan Mira 3 LMH microscope. Before observations, the powders were ultrasonically dispersed in ethanol, deposited onto a carbon-coated aluminium stub and sputtered with a thin conductive Au/Pd layer. For each composition, several representative micrographs at different magnifications were recorded to visualize both the agglomerate structure and the underlying primary particles. Particle size distributions were obtained by measuring the equivalent circle diameters of at least 400 – 500 particles using the ImageJ software. The resulting histograms were fitted by log-normal functions to determine the average particle diameter $\langle D \rangle$ and the standard deviation for each f value.

In addition to SEM-based measurements, the hydrodynamic size of particles in suspension was evaluated by dynamic light scattering. For this purpose, the powders were dispersed in distilled water with a small addition of ethanol and 0.1 wt.% sodium dodecyl sulfate as a surfactant, followed by ultrasonication for 15 min in an ultrasonic bath. The measurements were carried out at room temperature in disposable polystyrene cuvettes, and the particle size distributions were obtained from the autocorrelation function of scattered light intensity assuming a spherical particle model. These data were used to assess the degree of agglomeration in the as-combusted powders and to compare with the SEM-derived particle size distributions.

The elemental composition and cation ratios in the synthesized ferrites were analyzed by energy-dispersive X-ray spectroscopy (EDX) using an Oxford Ultim MAX 100 detector attached to the SEM. For each sample, spectra were acquired from several regions with an area of 50 – 100 μm^2 to obtain statistically reliable results. Quantitative analysis was performed using the manufacturer's software with ZAF corrections, and the obtained atomic fractions of Mn, Zn and Fe were compared with the nominal stoichiometry. Special attention was paid to the possible presence of impurity cations or secondary phases; however, within the detection limit of the method no significant deviations from the nominal composition were observed.

Magnetic properties of $Zn_{0.5}Mn_{0.5}Fe_2O_4$ nanopowders were studied using a Lake Shore vibrating sample magnetometer. Room-temperature hysteresis loops were recorded in external magnetic fields from -400 to $+400$ Oe. Prior to measurements, the powders were pressed into small cylindrical pellets and fixed in a non-magnetic sample holder to minimize mechanical vibrations. The magnetization was measured as a function of applied field with a step of 10 Oe near the coercive region and 50 – 100 Oe at higher fields. The experimental $M(H)$ loops were further processed using MeasureLINK-MCS and Curve Handler software. From the corrected loops, the saturation magnetization M_s, remanent magnetization M_r and coercive field H_c were determined according to standard procedures. All magnetic parameters were normalized to the mass of the sample measured with accuracy better than 0.1 mg.

For convenience, the samples synthesized at different fuel-to-oxidizer ratios are hereafter denoted as $f = 0.4, 0.6, 0.8, 1.0, 1.2, 1.4$ and 1.6, respectively. All processing parameters (solution volumes, heating profiles, dispersion conditions and measurement settings) were kept identical for the whole series so that the only intentional variable was the value of f. This approach makes it possible to attribute the observed differences in microstructure and magnetic response directly to the change in redox conditions during combustion, rather than to uncontrolled variations in post-synthesis treatment.

3. Results and discussion

The SEM micrographs in Fig. 1(a–g) demonstrate that all $Zn_{0.5}Mn_{0.5}Fe_2O_4$ powders obtained by glycine-nitrate combustion consist of highly porous, weakly sintered agglomerates formed by much finer primary particles. At low magnification, the powders appear as irregular flakes or cauliflower-like granules with typical sizes of several micrometres

(5 – 20 μm). The agglomerates are rather fragile and easily fragmented during sample preparation, which is consistent with the loose, foamy character of combustion products. Higher-magnification insets reveal that the surface of these agglomerates is built from nearly equiaxed nanoparticles with sizes of a few tens of nanometres; these observations correlate well with the particle size distributions discussed below.

Despite the variation of the fuel-to-oxidizer ratio, the overall morphology of the powders remains qualitatively similar. For the most fuel-lean composition (sample a, $f = 0.4$) the agglomerates are relatively compact, with a plate-like shape and a moderately developed system of interparticle pores. The primary particles in this sample tend to form contiguous clusters and necks, indicating partial sintering during the comparatively mild combustion process. In contrast, increasing f to 0.6 (sample b) leads to more open, sponge-like agglomerates with large voids and thin walls. Such morphology suggests a more vigorous gas evolution and higher local combustion temperature, which promote fast expansion of the reacting mass and generate a finer internal texture.

Near the stoichiometric mixture ($f = 0.8$ and 1.0, samples c and d) the powders retain a highly porous structure, but the agglomerates become more rounded and their surface is covered by densely packed nanoparticles. The insets show that the primary particles are relatively uniform in size and exhibit smooth faceted outlines, indicating improved crystallinity. The voids inside the agglomerates are more homogeneous and form a network of channels that can facilitate mass transport during subsequent sintering. Such morphology is favourable for obtaining dense ceramics at reduced temperatures.

For fuel-rich mixtures ($f \geq 1.2$, samples e–g) the morphology again changes slightly. Sample e ($f = 1.2$) still shows loose flake-like agglomerates, but their surface becomes rougher, and some regions contain fused clusters of nanoparticles, presumably due to local overheating. In sample f ($f = 1.4$) nearly spherical granules with a relatively smooth outer shell are observed against a background of fine powder. These globular agglomerates likely originate from partial melting and shrinkage of the combustion foam when the reaction temperature is close to, or exceeds, the softening point of the oxide skeleton. For the highest fuel content ($f = 1.6$, sample g) the agglomerates again acquire an elongated cauliflower-like shape; their surface is covered with compact aggregates of nanoparticles, while the inner porosity becomes somewhat less pronounced, which may indicate enhanced sintering in the hottest combustion conditions.

Energy-dispersive X-ray analysis summarized in the table on the left of Fig. 1 confirms that, regardless of the redox conditions, the cation composition of all samples is close to the nominal $Zn_{0.5}Mn_{0.5}Fe_2O_4$ stoichiometry. The Mn and Zn contents vary in narrow ranges around 17 at.% each, whereas the Fe content remains close to 65 at.% for all specimens. These small deviations are within the typical experimental uncertainty of EDX measurements for light elements and do not show any systematic trend with f. Furthermore, no regions enriched in a particular cation were detected in mapping mode, which indicates a good macroscopic homogeneity of the combustion-derived powders and the absence of large segregated secondary phases, in agreement with the XRD data.

Thus, SEM observations reveal that varying the fuel-to-oxidizer ratio in the glycine-nitrate system does not radically change the general foamy morphology of the Zn–Mn ferrite powders, but noticeably influences the degree of porosity, the shape of agglomerates and the extent of local sintering. Fuel-lean mixtures produce somewhat denser plate-like agglomerates, while stoichiometric and moderately fuel-rich compositions yield highly porous, uniform foam structures composed of well-crystallized nanoparticles. At very high fuel contents partial collapse and rounding of the agglomerates occur, reflecting more intense combustion. These morphological features, combined with the essentially constant cation stoichiometry, provide a basis for understanding the trends in particle size distributions and magnetic properties discussed in the following sections.

Figure 2 summarizes the particle size distributions of the $Zn_{0.5}Mn_{0.5}Fe_2O_4$ powders derived from the SEM images in Fig. 1. In all cases the histograms can be satisfactorily fitted by a single log-normal function, indicating that the powders consist mainly of one population of primary particles and that no pronounced bimodality is introduced by the combustion process. The distributions are moderately narrow, with most particles lying in the 40 – 130 nm range, and only a small fraction of larger particles forming a long tail attributed to limited neck growth or local aggregation.

For the fuel-lean composition ($f = 0.4$, Fig. 2a) the average particle diameter is $\langle D \rangle = 66.6$ nm, with a symmetric distribution centered at 60 – 70 nm. A slight decrease of $\langle D \rangle$ to 63.2 nm is observed when the fuel content is increased to $f = 0.6$ (Fig. 2b); in this case the peak becomes somewhat sharper and shifts to smaller diameters, consistent with a more fragmented, highly porous morphology. The largest particles are obtained near the stoichiometric redox ratio. For $f = 0.8$ and 1.0 (Fig. 2(c,d)) the mean diameters rise to 85.1 and 87.7 nm, respectively, and the histograms broaden towards 120 – 180 nm, reflecting more intensive growth and partial coalescence of crystallites under the hottest and longest-lasting combustion conditions.

Further increase of the fuel content leads again to a reduction of the particle size. For $f = 1.2$ (Fig. 2e) the mean value drops to 74.8 nm, while for $f = 1.4$ the smallest particles in the series are obtained, with $\langle D \rangle = 56.3$ nm and a relatively narrow peak located around 50 – 60 nm (Fig. 2f). At the highest fuel ratio ($f = 1.6$, Fig. 2g) the distribution broadens slightly and $\langle D \rangle$ increases to 62.1 nm, indicating some coarsening but still remaining below the values for the stoichiometric mixtures.

The data demonstrate a non-monotonic dependence of particle size on the fuel-to-oxidizer ratio: the powders prepared under stoichiometric conditions are coarser, whereas both fuel-deficient and strongly fuel-rich mixtures yield finer

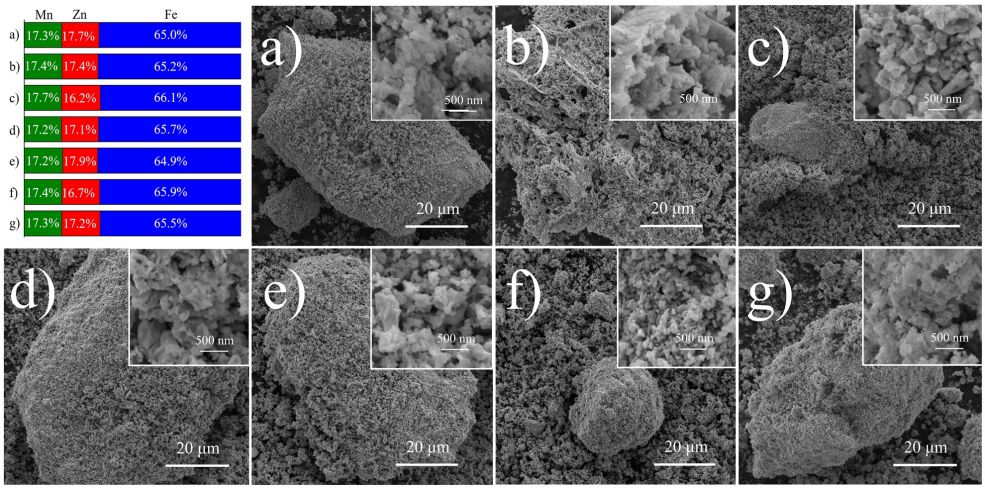

FIG. 1. SEM micrographs of $Zn_{0.5}Mn_{0.5}Fe_2O_4$ powders obtained by glycine-nitrate combustion at different fuel-to-oxidizer ratios: (a) $f = 0.4$, (b) 0.6, (c) 0.8, (d) 1.0, (e) 1.2, (f) 1.4 and (g) 1.6 (main images – agglomerates, insets – primary particles). The table on the left summarizes the EDX-derived cation composition for each sample, confirming stoichiometry close to the nominal $Zn_{0.5}Mn_{0.5}Fe_2O_4$

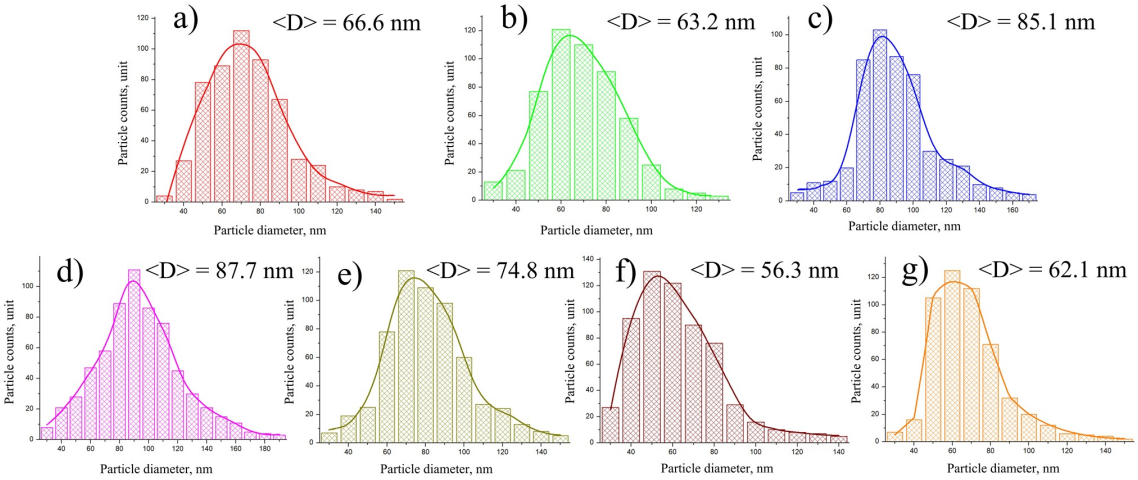

FIG. 2. Particle size distributions of $Zn_{0.5}Mn_{0.5}Fe_2O_4$ nanoparticles obtained by glycine-nitrate combustion at different fuel-to-oxidizer ratios f, constructed from SEM micrographs in Fig. 1: (a) $f = 0.4$, $\langle D \rangle = 66.6$ nm; (b) $f = 0.6$, $\langle D \rangle = 63.2$ nm; (c) $f = 0.8$, $\langle D \rangle = 85.1$ nm; (d) $f = 1.0$, $\langle D \rangle = 87.7$ nm; (e) $f = 1.2$, $\langle D \rangle = 74.8$ nm; (f) $f = 1.4$, $\langle D \rangle = 56.3$ nm; (g) $f = 1.6$, $\langle D \rangle = 62.1$ nm. Solid lines represent log-normal fits to the experimental histograms

nanoparticles. This behaviour can be rationalized by the competition between combustion temperature, gas evolution and quenching rate. The observed trends in $\langle D \rangle$ will directly influence the magnetic properties discussed below, since they determine the balance between single-domain behaviour and interparticle interactions in the nanoferrite powders.

Figure 3 combines the X-ray diffraction patterns of the $Zn_{0.5}Mn_{0.5}Fe_2O_4$ powders (left) with the crystallite size distributions obtained from line-broadening analysis (right), thus providing an integral picture of their structural evolution with changing fuel-to-oxidizer ratio f. The diffraction patterns of all samples exhibit a set of well-resolved reflections that can be indexed to a single cubic spinel phase with space group $Fd\bar{3}m$. The most intense peaks correspond to the (220), (311), (400), (422), (511) and (440) planes, positioned at Bragg angles characteristic of Mn–Zn ferrites. No additional reflections attributable to secondary oxide phases such as Fe_2O_3, MnO_x or ZnO are detected within the experimental sensitivity, and the diffuse background remains low, indicating that the amount of amorphous material does not exceed a few percent. This confirms that glycine-nitrate combustion followed by a mild calcination step is sufficient to produce phase-pure Zn–Mn ferrite over the whole range of redox conditions explored.

Although the phase composition is identical, the peak profiles and relative intensities exhibit noticeable changes with f. The pattern of the most fuel-lean sample ($f = 0.4$) shows the broadest reflections and somewhat lower peak intensities, suggesting a smaller average crystallite size and/or higher microstrain in this powder. At the same time, a slight increase of background at low angles can be seen, which may be associated with a minor amorphous fraction formed under

less exothermic combustion conditions. As the fuel content is increased to $f = 0.6 – 1.0$, the diffraction peaks become significantly sharper and more intense, reflecting improved crystallinity and growth of coherently diffracting domains. For the stoichiometric mixture ($f = 1.0$) the reflections, especially (311), are the narrowest in the series, consistent with the highest combustion temperature and longest effective dwelling time in the reaction front. Further enrichment in fuel ($f = 1.2 – 1.6$) results in a moderate broadening again, pointing to partial refinement of crystallites and possibly an increase of lattice defects caused by more violent gas release and faster quenching of the reaction products. No appreciable systematic shift of the main peaks is observed by eye, which implies that variations of the lattice parameter with f are rather subtle and will be quantified in the next figure.

The right-hand panel of Fig. 3 presents the size distributions of the coherently diffracting domains derived from the XRD data using a model assuming log-normal statistics. All distributions are unimodal, indicating that each powder is characterized by a dominant crystallite size rather than a superposition of several populations. For the fuel-deficient sample ($f = 0.4$, red curve) the distribution is very narrow and centered at relatively small sizes, on the order of a few tens of nanometres; this agrees with the pronounced peak broadening seen in its diffraction pattern. The high density of small crystallites is expected for a combustion route with reduced heat release, where the temperature is insufficient to drive extensive domain growth.

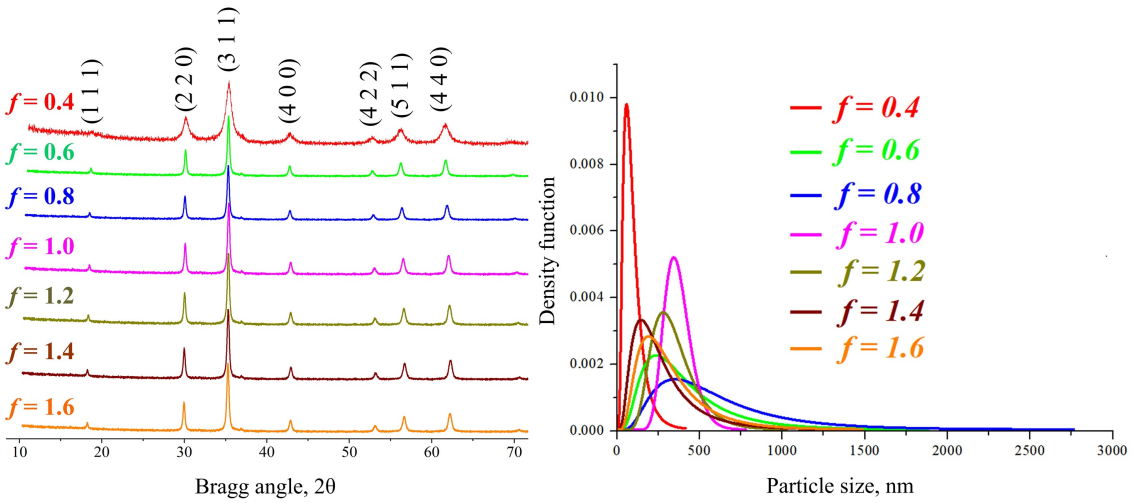

FIG. 3. (a) X-ray diffraction patterns of $Zn_{0.5}Mn_{0.5}Fe_2O_4$ powders synthesized by glycine-nitrate combustion at different fuel-to-oxidizer ratios $f = 0.4 – 1.6$, showing single-phase cubic spinel structure; (b) corresponding crystallite size distributions obtained from XRD line-broadening analysis and fitted with log-normal functions

When the fuel content is adjusted to $f = 0.6$ and 0.8 (green and blue curves), the distributions broaden and their maxima shift to larger sizes, reaching several hundred nanometres for the nearly stoichiometric composition. The long right-hand tails extending up to the micrometre range are indicative of a small fraction of oversized domains or strongly coalesced crystallites that have grown at the highest local temperatures inside the combustion front. This tendency correlates with the narrowing of the diffraction peaks and reflects more effective coarsening under near-stoichiometric conditions.

At even higher fuel ratios ($f = 1.2 – 1.6$, olive, brown and orange curves) the mode of the distribution's shifts back towards smaller crystallite sizes and the high-size tail becomes less pronounced. In other words, strongly fuel-rich mixtures yield a microstructure in which the majority of domains are significantly finer than in the stoichiometric case, despite the overall exothermicity of the reaction being higher. Such behaviour can be explained by the competing influence of rapid gas evolution and quenching: very intense combustion generates highly expanded foam that cools down quickly, limiting the time available for crystal growth and favouring the formation of numerous small domains. At the same time, the presence of some broader distributions for these samples suggests an increased contribution of defect-rich or strained crystallites.

The XRD patterns and crystallite size distributions in Fig. 3 demonstrate that the Red/Ox ratio in the glycine-nitrate system is a powerful tool for tuning the structural state of $Zn_{0.5}Mn_{0.5}Fe_2O_4$ nanopowders. All compositions remain single-phase cubic spinel, but the average size of coherently diffracting domains and the width of their distributions change in a non-monotonic manner: fuel-lean and strongly fuel-rich conditions produce finer crystallites, whereas mixtures close to stoichiometric favour their growth and partial coalescence. These structural differences are expected to have a direct impact on the magnetic behaviour of the powders, influencing both saturation magnetization and coercivity through the balance between single-domain and multi-domain particles and the level of lattice strain.

Figure 4 summarizes how the main structural parameters of the $Zn_{0.5}Mn_{0.5}Fe_2O_4$ powders depend on the fuel-to-oxidizer ratio f. The red symbols represent the average crystallite size D obtained from XRD line-broadening analysis,

the green symbols show the lattice parameter a, and the blue symbols correspond to the lattice microstrain β. Together, these data provide a quantitative description of how the redox conditions during combustion control the structural state of the ferrite.

The crystallite size exhibits a pronounced non-monotonic behaviour with f. For the most fuel-lean mixture ($f = 0.4$) the crystallite size is very small, on the order of 8 – 10 nm, which is consistent with the strong peak broadening in the corresponding diffraction pattern and with the fine microstructure observed by SEM. Such small domains are typical for combustion reactions proceeding at relatively low adiabatic temperatures, where the energy released is sufficient to form the spinel phase but insufficient for extensive grain growth. When f increases to 0.6 and 0.8, D rises steeply to ∼35 and ∼60 nm, respectively, reflecting the enhancement of flame temperature and the longer time available for coarsening of the oxide skeleton. The maximum crystallite size (∼75 – 80 nm) is reached at $f = 1.0$, i.e. under almost stoichiometric redox conditions, where the balance between heat release and gas evolution is optimal for growth of coherently diffracting domains. A further increase of fuel content leads to a gradual refinement of the structure: D decreases to ∼50 nm at $f = 1.2$, reaches a local minimum of ∼20 – 25 nm at $f = 1.4$ and then slightly increases again to ∼40 nm at $f = 1.6$. This reduction in crystallite size at high f is attributed to more violent gas evolution and faster quenching of the combustion foam, which freeze the structure before large domains can form.

The variation of the lattice parameter a with f is less pronounced but still clearly systematic. For $f = 0.4$ the lattice constant is close to 8.418 – 8.420 Å. Upon increasing f to 0.6 and 0.8, a grows to ∼8.435 and ∼8.450 Å, respectively, and reaches a maximum of about 8.453 – 8.454 Å for the stoichiometric mixture. With further fuel enrichment the lattice parameter slightly decreases, remaining in the range 8.445 – 8.452 Å. These modest changes can be related to a subtle modification of cation valence states and distribution between tetrahedral and octahedral sites, caused by differences in local oxygen partial pressure and cooling rate. Fuel-lean conditions favour a more oxidizing environment and may increase the fraction of smaller Fe^{3+} and Mn^{3+} cations, leading to a contracted lattice. Near-stoichiometric combustion, where the temperature is highest and the redox balance is closer to equilibrium, promotes a configuration with a larger average ionic radius and thus a larger unit cell. In very fuel-rich mixtures partial reduction of iron and manganese and the formation of oxygen vacancies may again reduce a.

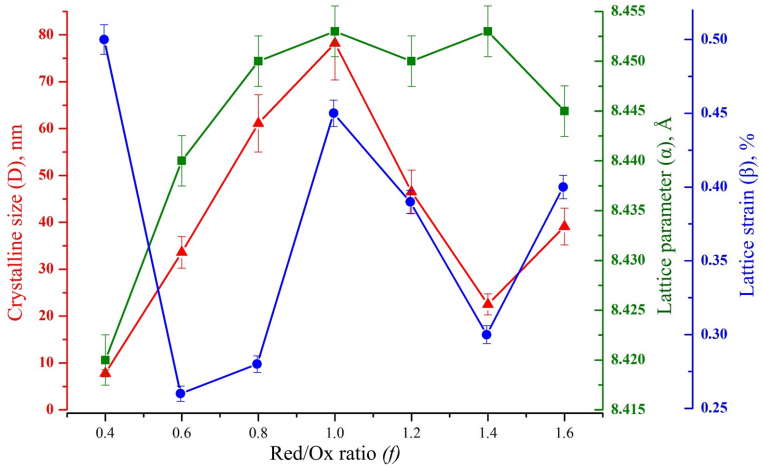

FIG. 4. (a) Dependence of crystallite size (D, red triangles, left axis), lattice parameter (a, green squares, middle axis) and lattice strain (β, blue circles, right axis) of $Zn_{0.5}Mn_{0.5}Fe_2O_4$ powders on the fuel-to-oxidizer ratio f, as obtained from XRD line-profile analysis

The microstrain β, plotted on the right axis, complements this picture. At $f = 0.4$ the strain is relatively high (∼0.47 – 0.50 %), indicating a considerable density of defects and local distortions in the small crystallites formed under fuel-deficient conditions. When f is increased to 0.6, β drops sharply to ∼0.26 %, reflecting more uniform crystallization and partial annealing of defects as the combustion temperature rises. For $f = 0.8$ and 1.0 the strain increases again up to ∼0.40 – 0.42 %, which may be associated with faster crystal growth and incorporation of non-equilibrium cation distributions into the lattice at the highest temperatures. In the fuel-rich region ($f \geq 1.2$) β shows a moderate minimum around $f = 1.4$ and then rises once more at $f = 1.6$, suggesting that intense gas evolution and rapid quenching introduce additional dislocations and lattice distortions even though the crystallite size is reduced.

Figure 4 demonstrates that the structural parameters of glycine-nitrate derived $Zn_{0.5}Mn_{0.5}Fe_2O_4$ are highly sensitive to the fuel-to-oxidizer ratio. Fuel-lean combustion yields very small, strongly strained crystallites with a slightly contracted lattice; near-stoichiometric conditions produce the largest domains and the maximum lattice parameter; strongly fuel-rich mixtures again lead to finer, more defective crystallites and a slight lattice contraction. These trends provide an important link between the combustion conditions and the magnetic behaviour of the powders, since both crystallite size and lattice strain critically influence saturation magnetization and coercivity in nanostructured ferrites.

Figure 5 presents the room-temperature magnetization curves $M(H)$ for the $Zn_{0.5}Mn_{0.5}Fe_2O_4$ nanopowders synthesized at different fuel-to-oxidizer ratios f. All samples exhibit typical S-shaped hysteresis loops that are narrow and symmetric with respect to the origin, confirming that the powders behave as soft ferrimagnetic materials. In the applied field range of ± 5 – 6 kOe the magnetization gradually approaches a quasi-saturation plateau, but does not reach a perfectly horizontal region, indicating that some spin canting and surface disorder remain in these nanostructured ferrites. The relatively small loop area for all compositions implies low hysteresis losses, which is advantageous for applications in low- and medium-frequency magnetic devices.

Despite the overall similarity of the loop shapes, there is a pronounced dependence of the magnetization level on the Red/Ox ratio. The fuel-lean sample with $f = 0.4$ displays the lowest saturation magnetization: its $M(H)$ curve lies well below the others and reaches only a modest magnetization even in the maximum applied field. This behaviour is consistent with its very small crystallite size and relatively high lattice strain, which enhance surface spin canting and disturb the long-range superexchange interactions between cations in the A and B sublattices. As f increases to 0.6 and 0.8 the loops shift upward; the powders synthesized near the stoichiometric composition ($f \approx 0.8$ – 1.0) show the highest magnetization values in the entire series. For these samples the steeper initial slope and higher magnetization at high fields indicate a more coherent alignment of spins, facilitated by larger crystallites and reduced fraction of magnetically disordered surface atoms. When the fuel content is further increased to 1.2 – 1.6, the magnetization at a given field slightly decreases again, in line with the partial refinement of crystallite size and the increased defect density inferred from the structural analysis.

The inset in Fig. 5 magnifies the low-field region around the origin, making it possible to compare coercivity and remanence for the different compositions. All loops intersect the magnetization axis at small positive and negative coercive fields, confirming their soft-magnetic character. Nevertheless, distinct trends with f can be identified. The sample synthesized at $f = 0.4$ shows the smallest coercive field and an almost linear passage through the origin, which is typical of very fine particles approaching the superparamagnetic or single-domain limit, where magnetization reversal occurs predominantly via coherent rotation and thermal activation. The remanent magnetization of this powder is also minimal, giving a very low M_r/M_s ratio ("squareness"), in agreement with the predominance of superparamagnetic-like particles and the wide distribution of anisotropy axes.

As the fuel-to-oxidizer ratio is increased to 0.6 – 1.0, the loops become progressively more "square": the intercept of the $M(H)$ curve with the magnetization axis at zero field moves to higher values, and the slope in the vicinity of the coercive field becomes steeper. This indicates an increase in the fraction of stable single-domain or small multi-domain grains with well-defined anisotropy, for which magnetization reversal proceeds via domain wall motion and nucleation. The coercivity in this region is moderate but clearly larger than for $f = 0.4$, reflecting the strengthening of magnetocrystalline anisotropy and pinning effects as crystallites grow and internal stresses redistribute. For fuel-rich compositions ($f \geq 1.2$) the loops slightly contract in width again, suggesting a partial reduction of coercive field, while the remanence remains at a relatively high level. Such behaviour can be attributed to the coexistence of smaller, more easily reversible particles with larger grains containing pinned domain walls, consistent with the bimodal structural features inferred from XRD and SEM.

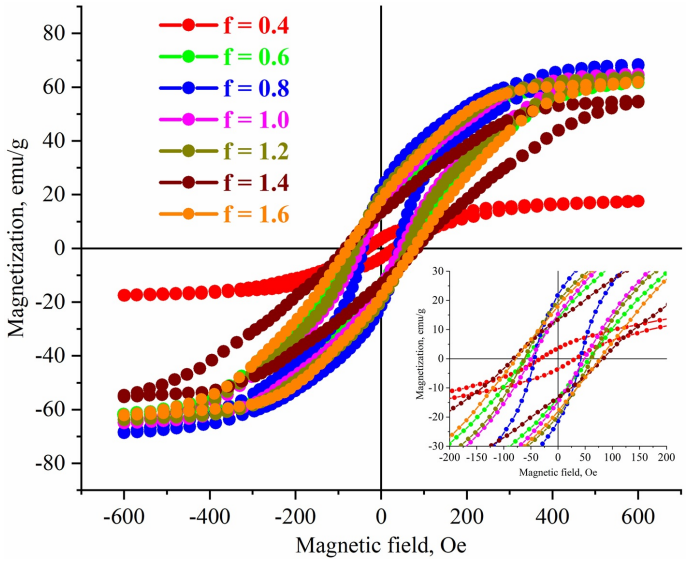

FIG. 5. (a) Room-temperature hysteresis loops $M(H)$ of $Zn_{0.5}Mn_{0.5}Fe_2O_4$ nanopowders synthesized by glycine–nitrate combustion at different fuel-to-oxidizer ratios ($f = 0.4$ – 1.6); inset shows an enlarged low-field region used to determine coercive field and remanent magnetization

Figure 5 demonstrates that the magnetic response of combustion-derived $Zn_{0.5}Mn_{0.5}Fe_2O_4$ nanopowders can be effectively tuned by varying the fuel-to-oxidizer ratio in the glycine-nitrate system. Fuel-lean conditions lead to very soft, weakly magnetized powders dominated by ultrafine, strongly disordered grains. Near-stoichiometric mixtures provide the highest magnetization and moderate coercivity, which is optimal for many soft-magnetic applications. Strongly fuel-rich conditions again decrease the magnetization and slightly reduce the coercivity, reflecting the complex interplay between crystallite size, lattice strain and cation distribution. The correlations between these magnetic characteristics and the structural parameters discussed earlier highlight the key role of combustion redox conditions in designing nanostructured Mn–Zn ferrites with tailored functional properties.

Figure 6 presents the quantitative magnetic parameters extracted from the hysteresis loops as a function of the fuel-to-oxidizer ratio f: (a) coercive field H_c, (b) remanent magnetization M_r and (c) saturation magnetization M_s. Together they illustrate how the redox conditions during combustion govern the softness and strength of the magnetic response of $Zn_{0.5}Mn_{0.5}Fe_2O_4$ nanopowders.

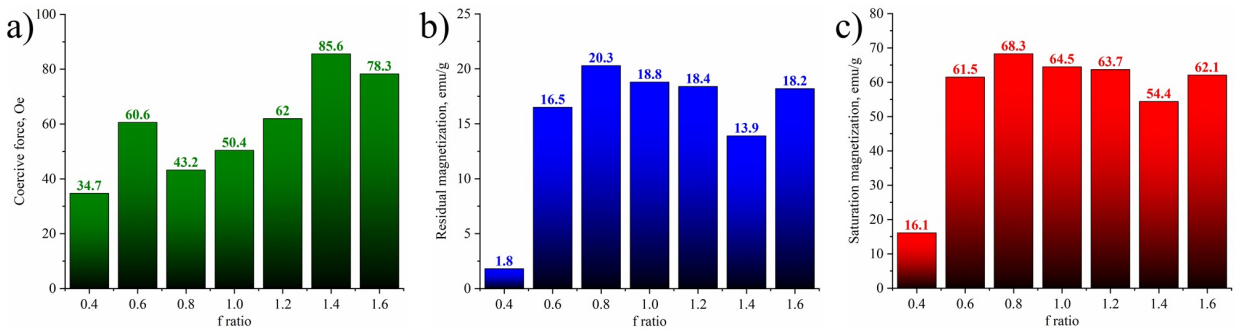

FIG. 6. (a) Dependence of (a) coercive field (H_c), (b) remanent magnetization (M_r) and (c) saturation magnetization (M_s) of $Zn_{0.5}Mn_{0.5}Fe_2O_4$ nanopowders on the fuel-to-oxidizer ratio f, obtained from the room-temperature hysteresis loops

The coercive field (Fig. 6a) shows a clear non-monotonic behaviour. For the fuel-lean sample ($f = 0.4$) H_c is only 34.7 Oe, indicating very easy magnetization reversal in a structure dominated by ultrafine, weakly interacting particles. Increasing f to 0.6 sharply raises H_c to 60.6 Oe, reflecting the growth of crystallites and strengthening of magnetocrystalline anisotropy and domain-wall pinning. At $f = 0.8$ and 1.0 the coercivity decreases to 43.2 and 50.4 Oe, respectively, suggesting that part of the grains become multidomain and magnetization reversal proceeds via more mobile walls. For fuel-rich compositions $f = 1.2$ – 1.6 the coercive field increases again, reaching a maximum of 85.6 Oe at $f = 1.4$ and slightly dropping to 78.3 Oe at $f = 1.6$. This rise is consistent with the refined, defect-rich microstructure produced under strongly exothermic, rapidly quenched combustion, where structural imperfections act as effective pinning centres.

The variation of M_r (Fig. 6b) follows a different trend. The fuel-lean sample has an extremely low remanence of 1.8 emu/g, in line with its nearly superparamagnetic-like behaviour and very small hysteresis loop. When the fuel ratio increases to 0.6 and 0.8, M_r rapidly grows to 16.5 and 20.3 emu/g, respectively, reflecting an increasing fraction of magnetically stable single-domain or small multidomain grains. In the range $f = 1.0$ – 1.2 the remanence remains high (18.8 – 18.4 emu/g), then drops to 13.9 emu/g at $f = 1.4$ and rises again to 18.2 emu/g at $f = 1.6$. The reduced M_r for $f = 1.4$ correlates with the smallest crystallite size and highest coercivity in this region, where stronger random anisotropy and more pronounced surface spin disorder partially cancel the net magnetization after field removal.

Saturation magnetization M_s (Fig. 6c) also exhibits a pronounced dependence on f. A very low value of 16.1 emu/g is obtained for the most fuel-deficient sample, confirming that extreme size reduction and high lattice strain strongly suppress long-range ferrimagnetic order. Near stoichiometry, M_s increases dramatically, reaching 61.5 emu/g at $f = 0.6$ and a maximum of 68.3 emu/g at $f = 0.8$. For $f = 1.0$ and 1.2 the saturation magnetization remains relatively high (64.5 and 63.7 emu/g), then decreases to 54.4 emu/g at $f = 1.4$ and partially recovers to 62.1 emu/g at $f = 1.6$. These changes mirror the structural evolution: larger, well-ordered crystallites formed at intermediate f minimize surface-spin canting and yield higher M_s, whereas both fuel-lean and highly fuel-rich regimes produce smaller, more defective particles with reduced magnetic moments.

Figure 6 highlights that an optimal fuel-to-oxidizer ratio around $f \approx 0.8$ – 1.0 provides a combination of high M_s and M_r with moderate H_c, characteristic of soft magnetic ferrites. Deviations towards too low or too high f lead either to weakly magnetized, almost superparamagnetic powders ($f = 0.4$) or to more coercive, defect-rich materials ($f \geq 1.4$), underscoring the key role of combustion redox conditions in tailoring the functional performance of Zn–Mn nanoferrites.

4. Conclusion

Nanostructured $Zn_{0.5}Mn_{0.5}Fe_2O_4$ powders were successfully synthesized by the glycine-nitrate solution combustion method with the fuel-to-oxidizer ratio varied in a wide range, $f = 0.4$ – 1.6. Regardless of the redox conditions, XRD

confirmed the formation of a single-phase cubic spinel, while SEM revealed highly porous agglomerates composed of nanosized primary particles with compositions close to the nominal stoichiometry. Systematic variation of f led to pronounced changes in crystallite size, lattice parameter and microstrain: fuel-lean and strongly fuel-rich mixtures produced finer, more strained crystallites with slightly contracted lattices, whereas near-stoichiometric conditions promoted the growth of larger domains and maximized the lattice constant.

These structural modifications were directly reflected in the magnetic response at 300 K. All samples exhibited soft-ferrimagnetic behaviour with relatively narrow hysteresis loops, but the absolute values of the magnetic parameters were strongly dependent on f. The saturation magnetization varied from 16.1 to 68.3 emu/g, the remanent magnetization from 1.8 to 20.3 emu/g and the coercive field from 34.7 to 85.6 Oe. The lowest M_s and M_r were obtained for the most fuel-deficient powder, where extreme refinement and high lattice strain suppress long-range ferrimagnetic order, whereas strongly fuel-rich mixtures showed increased coercivity due to microstructural refinement and defect-induced pinning. The optimal combination of high M_s and M_r with moderate H_c, characteristic of soft magnetic ferrites, was achieved for $f \approx 0.8 - 1.0$, where crystallites are relatively large and structurally well ordered.

Overall, the results demonstrate that the fuel-to-oxidizer ratio in glycine–nitrate combustion is an efficient control parameter for tailoring both structural and magnetic characteristics of Zn–Mn nanoferrites. By selecting appropriate redox conditions, it is possible to obtain nanopowders with a desired balance between crystallite size, lattice strain and magnetic softness, which is crucial for further processing into low-loss cores and functional layers for electromagnetic devices. The established structure–property correlations provide a useful guideline for designing combustion-derived ferrites for power electronics, microwave absorbers and other soft-magnetic applications.

References

[1] Ott G., Wrba J., Lucke R., Recent developments of Mn–Zn ferrites for high permeability application. *J. of Magnetism and Magnetic Materials*, 2003, **254–255**, P. 535–537.

[2] Chen Z., Li T., Wang A., Shi M., Han B., The latest research progress on MnZn ferrite and their applications. *Open Ceramics*, 2025, **21**, 100732.

[3] Thakur P., Chahar D., Taneja S., Bhalla N., Thakur A., A review on MnZn ferrites: Synthesis, characterization and applications. *Ceramics International*, 2020, **46** (10), P. 15740–15763.

[4] Bai Y.-H., Xia Q.-H., Zhang D.-Y., Mn–Zn ferrite foam concrete: Enhanced electromagnetic wave absorption and pore structure by incorporating carbon fibers. *Ceramics International*, 2024, **50** (14), P. 25578–25597.

[5] Arulmurugan R., Vaidyanathan G., Sendhilnathan S., Jeyadevan B., Mn–Zn ferrite nanoparticles for ferrofluid preparation: Study on thermal–magnetic properties. *J. of Magnetism and Magnetic Materials*, 2006, **298** (2), P. 83–94.

[6] Slavu L.M., Rinaldi R., Corato R.D., Application in nanomedicine of Manganese-Zinc ferrite nanoparticles. *Applied Sciences*, 2021, **11** (23), 11183.

[7] Mathew D.S., Juang R.-S., An overview of the structure and magnetism of spinel ferrite nanoparticles and their synthesis in microemulsions. *Chemical Engineering J.*, 2007, **129** (1–3), P. 51–65.

[8] Deepty M., Srinivas C., Mohan N.K., Kumar E.R., Singh S., Meena S.S., Bhatt P., Sastry D.L., Chemical synthesis of Mn–Zn magnetic ferrite nanoparticles: Effect of secondary phase on extrinsic magnetic properties of Mn–Zn ferrite nanoparticles. *Ceramics International*, 2024, **50** (11), P. 18446–18453.

[9] Etemadi H., Plieger P.G., Synthesis and characterisation of $M_xFe_{3-x}O_4$ (M = Fe, Mn, Zn) spinel nanoferrites through a solvothermal route. *J. of Materials Science*, 2021, **56**, P. 17568–17583.

[10] Jiang H., Xu X., Zhang R., Zhang Y., Chen J., Yang F., Nano ferrites (AFe_2O_4, A = Zn, Co, Mn, Cu) as efficient catalysts for catalytic ozonation of toluene. *RSC Advances*, 2020, **10**, P. 5116–5128.

[11] Dyachenko S.V., Martinson K.D., Cherepkova I.A., Zhernovoi A.I., Particle size, morphology, and properties of transition metal ferrospinels of the MFe_2O_4 (M = Co, Ni, Zn) type, produced by glycine-nitrate combustion. *Russian J. of Applied Chemistry*, 2016, **89** (4), P. 535–539.

[12] Praveena K., Sadhana K., Bharadwaj S., Murthy S.R., Development of nanocrystalline Mn–Zn ferrites for high frequency transformer applications. *J. of Magnetism and Magnetic Materials*, 2009, **321** (16), P. 2433–2437.

[13] Kaewmanee T., Phuruangrat A., Thongtem T., Thongtem S., Solvothermal synthesis of Mn–Zn Ferrite(core)@SiO_2(shell)/$BiOBr_{0.5}Cl_{0.5}$ nanocomposites used for adsorption and photocatalysis combination. *Ceramics International*, 2020, **46** (3), P. 3655–3662.

[14] Martinson K.D., Kozyritskaya S.S., Panteleev I.B., Popkov V.I., Low coercivity microwave ceramics based on LiZnMn ferrite synthesized via glycine-nitrate combustion. *Nanosystems: Physics, Chemistry, Mathematics*, 2019, **10** (3), P. 313–317.

[15] Hu Y., Zou B., Xing H., Liu J., Chen Q., Wang X., Li L., Preparation of Mn–Zn ferrite ceramic using stereolithography 3D printing technology. *Ceramics International*, 2022, **48** (5), P. 6923–6932.

[16] Jain S.K., Dolia S.N., Choudhary B.L., Prashant B.L., Structural and morphological study of $Zn_{0.9}Mn_{0.05}Fe_{0.05}O$ synthesized by sol-gel wet chemical precipitation route. *IOP Conference Series: Materials Science and Engineering*, 2018, **348**, 012004.

[17] Venkatachalapathy R., Manoharan C., Venkateshwarlu M., Elfadeel G.A., Saddeek Y., Solution combustion route for Ni and Al co-doped lithium ferrite nanoparticles: Synthesis, the effect of doping on the structural, morphological, optical, and magnetic properties. *Ceramics International*, 2023, **49** (4), P. 6594–6607.

[18] Martinson K.D., Ivanov A.A., Panteleev I.B., Popkov V.I., Effect of sintering temperature on the synthesis of LiZnMnFe microwave ceramics with controllable electro/magnetic properties. *Ceramics International*, 2021, **47** (21), P. 30071–30081.

[19] Smirnova M.N., Nikiforova G.E., Kondrat'eva O.N., Synthesis of magnesium ferrite by combustion of glycine-nitrate gel: the influence of reagents on the gel-precursor and the microstructure of nanopowders. *Nanosystems: Physics, Chemistry, Mathematics*, 2024, **15** (2), P. 224–232.

[20] Saukhimov A.A., Hobosyan M.A., Dannagoda G.C., Zhumabekova N.N., Almanov G.A., Kumekov S.E., Martirosyan K.S., Solution-combustion synthesis and magnetodielectric properties of nanostructured rare earth ferrites. *International J. of Self-Propagating High-Temperature Synthesis*, 2015, **24**, P. 63–71.

[21] Martinson K.D., Sakhno D.D., Belyak V.E., Kondrashkova I.S., $Ni_{0.4}Zn_{0.6}Fe_2O_4$ Nanopowders by Solution-Combustion Synthesis: Influence of Red/Ox Ratio on their Morphology, Structure, and Magnetic Properties. *Int. J. of Self-Propagating High-Temperature Synthesis*, 2020, **29** (4), P. 202–207.

[22] Hwang C.-C., Tsai J.S., Huang T.-H., Combustion synthesis of Ni–Zn ferrite by using glycine and metal nitrates—investigations of precursor homogeneity, product reproducibility, and reaction mechanism. *Materials Chemistry and Physics*, 2005, **93** (2–3), P. 330–336.
[23] Nadargi D., Umar A., Nadargi J., Patil J., Mulla I., Akbar S., Suryavanshi S., Spinel Magnesium Ferrite ($MgFe_2O_4$): A Glycine-Assisted Colloidal Combustion and Its Potentiality in Gas-Sensing Application. *Chemosensors*, 2022, **10** (9), 361.
[24] Popkov V.I., Chebanenko M.I., Tenevich M.I., Buryanenko I.V., Semenov V.G., Solution combustion synthesis of iron-deficient $Sc_{2-x}Fe_xO_3$ ($x = 0.17$ – 0.47) nanocrystals with bixbyite structure: The effect of spatial constraints. *Ceramics International*, 2022, **48** (24), P. 36046–36055.
[25] Siddique F., Gonzalez-Cortes S., Mirzaei A., Xiao T., Rafiq M.A., Zhang X., Solution combustion synthesis: the relevant metrics for producing advanced and nanostructured photocatalysts. *Nanoscale*, 2022, **14**, P. 11806–11868.
[26] La P., Lei W., Wang X., Wei Y., Ma Y., Effects of excess $NaClO_4$ on phases, size and magnetic properties of Ni–Zn ferrite powders prepared by combustion synthesis. *Ceramics International*, 2015, **41** (8), P. 9843–9848.
[27] Martinson K.D., Belyak V.E., Sakhno D.D., Ivanov A.A., Lebedev L.A., Nefedova L.A., Panteleev I.B., Popkov V.I. Solution combustion assisted synthesis of ultra-magnetically soft LiZnTiMn ferrite ceramics. *J. of Alloys and Compounds*, 2022, **894**, 162554.
[28] Ortiz-Quinonez J.-L., Pal U., Villanueva M.S. Structural, Magnetic, and Catalytic Evaluation of Spinel Co, Ni, and Co–Ni Ferrite Nanoparticles Fabricated by Low-Temperature Solution Combustion Process. *ACS Omega*, 2018, **3** (11), P. 14986–15001.
[29] Azadmanjiri J. Preparation of Mn–Zn ferrite nanoparticles from chemical sol–gel combustion method and the magnetic properties after sintering. *J. of Non-Crystalline Solids*, 2007, **353** (44–46), P. 4170–4173.
[30] Kumar E.R., Jayaprakash R., The role of fuel concentration on particle size and dielectric properties of manganese substituted zinc ferrite nanoparticles. *J. of Magnetism and Magnetic Materials*, 2014, **366**, P. 33–39.
[31] Kumar E.R., Jayaprakash R., Effect of combustion rate and annealing temperature on structural and magnetic properties of manganese substituted nickel and zinc ferrites. *J. of Magnetism and Magnetic Materials*, 2013, **348**, P. 93–100.
[32] Varma A., Mukasyan A.S., Rogachev A.S., Manukyan K.V., Solution Combustion Synthesis of Nanoscale Materials. *Chemical Reviews*, 2016, **116** (23), P. 14493–14586.
[33] Ahmia N, Benamira M., Messaadia L., Masmoudi R., Horwat D., Avramova I., Sol-gel auto-combustion synthesized $ZnMn_2O_4$ for efficient photocatalytic Congo red degradation: structural, kinetics, computational, and ecotoxicity analyses. *J. of Physics and Chemistry of Solids*, 2026, **208**, 113038.
[34] Abdo M.A., Al-Wafi R., AlHammad M.S., Highly efficient visible light driven photocatalytic activity of rare earth cerium doped zinc-manganese ferrite: Rhodamine B degradation and stability assessment. *Ceramics International*, 2023, **49** (17), P. 29245–29258.
[35] Ivanovskaya M.I., Tolstik A.I., Kotsikau D.A., Pankov V.V., The structural characteristics of Zn-Mn ferrite synthesized by spray pyrolysis. *Russian J. of Physical Chemistry A*, 2009, **83**, P. 2081–2086.
[36] Ghodake U.R., Chaudhari N.D., Kambale R.C., Patil J.Y., Suryavanshi S.S., Effect of Mn^{2+} substitution on structural, magnetic, electric and dielectric properties of Mg–Zn ferrites. *J. of Magnetism and Magnetic Materials*, 2016, **407**, P. 60–68.
[37] Deraz N.M., Alarifi A., Preparation and characterization of nano-magnetic $Mn_{0.5}Zn_{0.5}Fe_2O_4$ system. *International J. of Electrochemical Science*, 2012, **7** (7), P. 5828–5836.

Submitted 2 December 2025; revised 9 December 2025; accepted 10 December 2025

Information about the authors:

Nikita Kiryanov – Saint Petersburg Electrotechnical University "LETI", Saint Petersburg, 199026, Russia; ORCID 0009-0000-8169-9287; nikyr@mail.ru

Kirill Martinson – Ioffe Institute, Politekhnicheskaya st., 26, Saint Petersburg, 194064, Russia; ORCID 0000-0001-9313-4267; martinsonkirill@mail.ru

Conflict of interest: the authors declare no conflict of interest.